

## **3.17% efficient $\text{Cu}_2\text{ZnSnS}_4$ - $\text{BiVO}_4$ integrated tandem cell for standalone overall solar water splitting**

Dingwang Huang<sup>a</sup>, Kang Wang<sup>a</sup>, Lintao Li<sup>a</sup>, Kuang Feng<sup>a</sup>, Na An<sup>c</sup>, Shigeru Ikeda<sup>b</sup>, Yongbo Kuang<sup>c</sup>, Yunhau Ng<sup>d</sup> and Feng Jiang<sup>a\*</sup>

- a. Institute of Semiconductor Science and Technology, South China Normal University, 55 Zhongshan Avenue West, Tianhe District, Guangzhou 510631, China
- b. Department of Chemistry, Konan University, 9-1 Okamoto, Higashinada, Kobe, Hyogo 658-8501, Japan
- c. Ningbo Institute of Industrial Technology, Chinese Academy of Science, Ningbo 315200, China
- d. School of Energy and Environment, City University of Hong Kong, Kowloon, Hong Kong 999077, China

\*email address: [fengjiangsolar@126.com](mailto:fengjiangsolar@126.com)

## **Experimental details**

### **Preparation of CZTS Films**

The CZTS films were prepared by spray pyrolysis method. The sprayed precursor solution was mixed by equal volume aqueous solution of  $\text{Cu}(\text{NO}_3)_2$  (17 mM),  $\text{Zn}(\text{NO}_3)_2$  (11.5 mM),  $\text{Sn}(\text{CH}_3\text{SO}_3)_2$  (11.5 mM) and thiourea  $\text{SC}(\text{NH}_2)_2$  (50 mM). In detail, The Cu-Zn stock solution was formed by 0.49 g  $\text{Cu}(\text{NO}_3)_2 \cdot 3\text{H}_2\text{O}$  and 0.41 g  $\text{Zn}(\text{NO}_3)_2 \cdot 6\text{H}_2\text{O}$  both dissolved in 40 mL pure water. Subsequently, the TU stock solution was formed by 0.46 g  $\text{SC}(\text{NH}_2)_2$  dissolved in 40 mL pure water. The Sn stock solution was formed by 550  $\mu\text{L}$   $\text{Sn}(\text{CH}_3\text{SO}_3)_2$  solution (50 wt.%) dissolved in 40 mL pure water, and the pH of this stock solution was adjusted to 1.5 by adding a few drops of concd nitric acid. Then, these three stock solutions were all separately stirred for at least two hours before their mix. The precursor solution was immediately sprayed onto

a cleaned Mo-coated soda-lime glass substrate preheated to 390°C. Then, the precursor film samples were vacuum sealed in a glass tube with 20 mg sulfur powder and subjected to sulfurization in a furnace at 590°C for 30 min. The preparation detail also could be reference to our previous similar papers.<sup>1,2</sup>

### **Surface Modification with HfO<sub>2</sub>/CdS/HfO<sub>2</sub> Sandwich Buffer Layers.**

An ultrathin HfO<sub>2</sub> layer was firstly deposited onto CZTS films by atomic layer deposition (ALD) method. HfO<sub>2</sub> was grown by using tetrakis (dimethylamido) hafnium as hafnium source and H<sub>2</sub>O as oxygen source. Based on our empirical value, the growth rate was estimated to be about 0.1 nm per cycle and the films were grown for 0, 3, 5 and 10 cycles at 250°C. The corresponding thicknesses of the HfO<sub>2</sub> layers were 0, 0.3, 0.5 and 1 nm respectively.

Furthermore, a CdS layer was deposited onto the HfO<sub>2</sub>/CZTS overlayer by the chemical bath deposition method (CBD). The prepared HfO<sub>2</sub>/CZTS overlayer was dipped into an aqueous solution containing 12.5 mM CdSO<sub>4</sub>, 0.22 mM SC(NH<sub>2</sub>)<sub>2</sub>, and 11 M NH<sub>4</sub>OH at 60°C for 15 min.

Ultimately, a HfO<sub>2</sub>/CdS/HfO<sub>2</sub> sandwich buffer layer was formed by depositing again a 60 ALD-cycles HfO<sub>2</sub> (6 nm) layer onto CdS/HfO<sub>2</sub>/CZTS overlayer.

### **Deposition of Pt Particles**

The Pt particles deposition was performed by using a three-electrode system consisting of HfO<sub>2</sub>/CdS/HfO<sub>2</sub>/CZTS as a working electrode, a Pt wire as a counter electrode, and Ag/AgCl as a reference electrode. These electrodes were put in 0.1 M Na<sub>2</sub>SO<sub>4</sub> solution containing 1 mM H<sub>2</sub>PtCl<sub>6</sub>, and the deposition was performed with a constant potential of -0.1 V<sub>VS. Ag/AgCl</sub> by using CHI660E electrochemical measurement unit. During the deposition process, the working electrode was illuminated by simulated AM 1.5G solar irradiation.

### **Preparation of BiVO<sub>4</sub> Photoanode**

The preparation details of the BiVO<sub>4</sub> samples could be reference to previous works by Kuang et al.<sup>3</sup> and Krol et al.<sup>4,5</sup>

### **Photoelectrochemical Measurements**

An online gas chromatography system (Shimadazu GC-2014 gas analyzer

equipped with a MS-5A column and a thermal conductivity detector) was used to detect H<sub>2</sub> and O<sub>2</sub> during the PEC water splitting. PEC H<sub>2</sub> generation from photocathodes was examined in a pH 6.5 phosphate buffer solution (0.2 M Na<sub>2</sub>HPO<sub>4</sub>/NaH<sub>2</sub>PO<sub>4</sub>) by using a standard solar simulator with AM 1.5G filter as a light source. The PEC cell was covered by a water jacket to maintain the temperature at 293 K. The two-electrode setup composed of the Pt-HfO<sub>2</sub>/CdS/HfO<sub>2</sub>/CZTS photocathode and a BiVO<sub>4</sub>-based photoanode in series connection was also employed to examine water splitting under the bias-free condition. Potentials referred to the Ag/AgCl electrode were converted to reversible hydrogen electrode using the Nernst equation:

$$V_{\text{RHE}} = V_{\text{Ag/AgCl}} + 0.059 \times \text{pH} + 0.199$$

ABPE was determined from the current density–potential response of the photocathodes by using the following equation:

$$\text{ABPE (\%)} = J \times V \times 100/P$$

Where J is the photocurrent density (mA/cm<sup>2</sup>), V is the applied potential (V<sub>RHE</sub>), and P is the intensity of simulated sunlight (100 mW/cm<sup>2</sup>).

### **Structural Characterization.**

Crystalline structures of the films were determined by X-ray diffraction (XRD), Raman spectroscopy and transmission electron microscopy (TEM) using a Rigaku Mini Flex X-ray diffractometer, a Jasco NRC 3100 laser Raman spectrophotometer and JEOL JEM-2100HR microscope respectively. Surface and cross section morphology were observed by scanning electron microscope (SEM) using Hitachi S-4800 microscope. Surface and bulk chemical structures of photoelectrodes were examined by X-ray photoelectron spectroscopy (XPS) using a Shimadzu AXIS ULTRA X-ray photo-electron spectrometer.

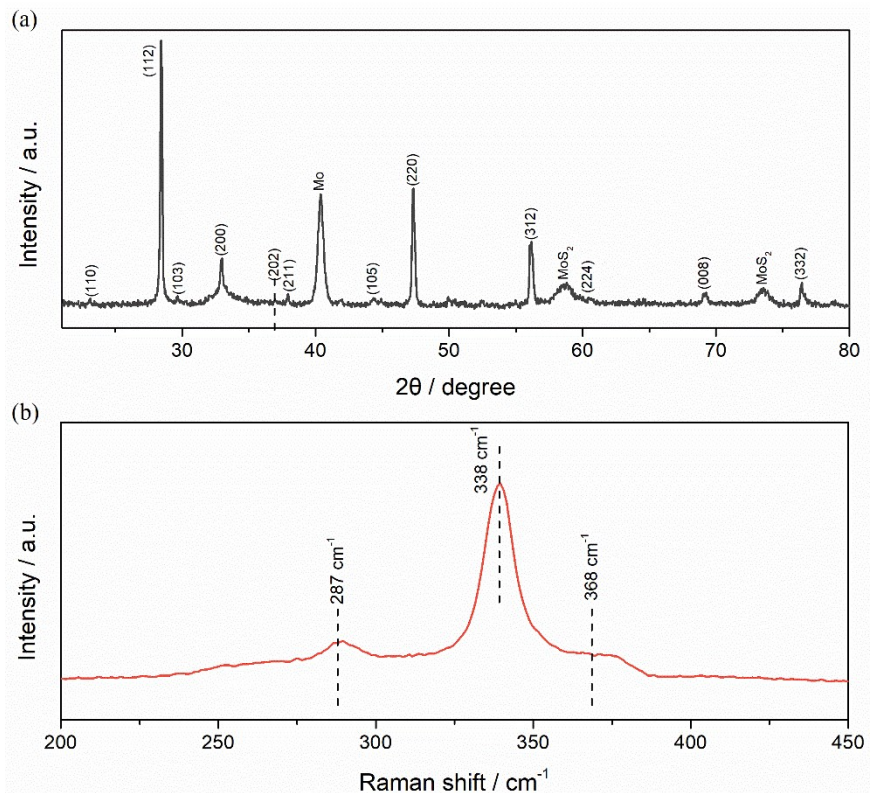


**Fig. S1:** (a) XRD patterns and (b) Raman spectrum of the CZTS film.

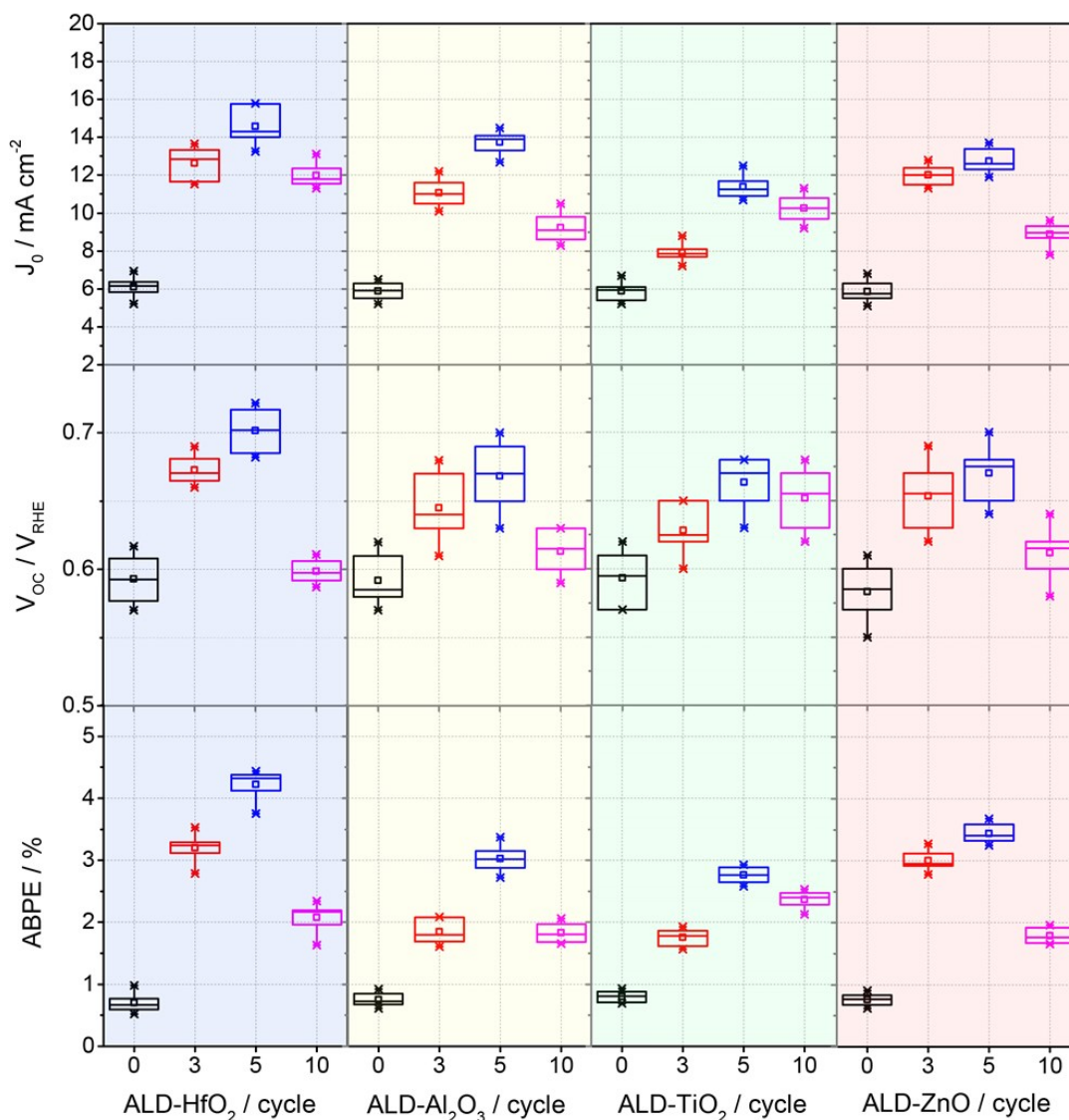


**Fig. S2:** Statistical box data of photoelectrochemical properties (photocurrent densities, photocurrent onset potential ( $V_{oc}$ ) and ABPE) of CZTS based photocathodes modified with  $HfO_2$ ,  $Al_2O_3$ ,  $TiO_2$  and  $ZnO$  intermediate layer as a function of their thickness (ALD cycles) at the interface of CdS/CZTS. The box plot denotes median (centre line), mean value (dots), 25th (bottom edge of the box), 75th (top edge of the box), 95th (upper whisker) and 5th (lower whisker) percentiles. The sample size in each column is 6 devices. The photocurrent onset potential ( $V_{oc}$ ) values were determined from the obvious inflection point where the photocurrent suddenly increases (excluding those significant spikes of photocurrent) of the chopped J-V curves.

We gave some possible mechanisms to explain why the  $HfO_2$  passivation layer is

superior according to some relevant literatures: Wang et al. reported that a ALD-HfO<sub>2</sub> interfacial passivation layer (IPL) can better optimized interface chemistry and improved electrical performance for sputtering-derived HfDyO<sub>x</sub> (HDO)/Si gate stack than Al<sub>2</sub>O<sub>3</sub> IPL, which was attributed to its larger permittivity, the negligible hysteresis, the small oxide charge density and the smallest gate leakage current density.<sup>6</sup> Xing et al pointed out that the NP-Si photocathode passivated by ALD-HfO<sub>2</sub> layer exhibits a started photocurrent density than that of TiO<sub>2</sub>/NP-Si, which is due to the advantages of the filed effect passivation and the chemical passivation from the HfO<sub>2</sub> layers.<sup>7</sup>

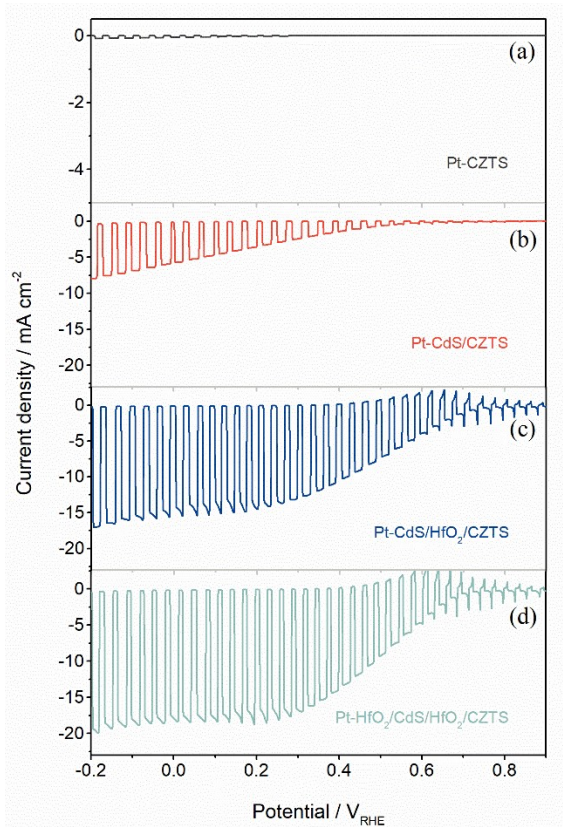


**Fig. S3:** Photocurrent density-potential curves of Pt-CZTS (a), Pt-CdS/CZTS (b), Pt-CdS/HfO<sub>2</sub>/CZTS (c) and Pt-HfO<sub>2</sub>/CdS/HfO<sub>2</sub>/CZTS (d) photocathodes measured in a 0.2 mol/dm<sup>3</sup> Na<sub>2</sub>HPO<sub>4</sub>/NaH<sub>2</sub>PO<sub>4</sub> solution (pH 6.5) under chopped solar simulated AM 1.5G light irradiation.

**Fig. S3a-d** show the photoelectrochemical performances of the Pt-CZTS, Pt-CdS/CZTS and Pt-CdS/HfO<sub>2</sub>/CZTS and Pt-HfO<sub>2</sub>/CdS/HfO<sub>2</sub>/CZTS samples under AM 1.5G solar light soaking. The Pt loaded CZTS photocathode did not present significant photocatalysis property i.e. the photocurrent and onset potential itself are very low.

However, adding CdS buffer layer under CZTS results in an appreciable enhancement in both photocurrent and onset potential, as expected from various similar systems reported by us and other researchers.<sup>1,8-11</sup> Photocurrent density at 0  $V_{\text{RHE}}$  as well as photocurrent onset potential of the present Pt-CdS/CZTS electrode at pH 6.5 reached  $-5.7 \text{ mA/cm}^2$  and  $0.59 V_{\text{RHE}}$ , respectively. However, photocorrosion nature of CdS seriously decreased the PEC stability of the CdS/CZTS photocathode. As shown in **Fig. S4**, the photocurrent detected under 0  $V_{\text{RHE}}$  of CdS/CZTS rapidly decreased from the original value of  $6 \text{ mA/cm}^2$  to  $1.2 \text{ mA/cm}^2$  in only 2 hours, that was caused by the photo oxidation of CdS which results in the dissolution and structure failure of CdS buffer under solar irradiation in solution.<sup>1,8</sup> Therefore, surface protection of CdS is a suitable way to prohibit its photocorrosion and dissolution into solution. Previously we used an ultra-thin  $\text{HfO}_2$  film to protect the surface of CdS and then efficiently enhanced the PEC stability of the CdS/CZTS based photocathode over 10 hours, and such ultra-thin  $\text{HfO}_2$  film was expected as a tunneling layer that facilitate the transfer of photoexcited carriers without recombination.<sup>1</sup> In this work, we insert a thin layer of  $\text{HfO}_2$  at the interface of CdS/CZTS and find that modification of  $\text{HfO}_2$  film at the interface between CZTS and CdS (i.e. interface of CdS/CZTS) could finally improve the photocurrent and fill factor (**Fig. S3c**), but the stability of Pt-CdS/ $\text{HfO}_2$ /CZTS photocathode still not good because no protective layer is added outside of the bare CdS (**Fig. S4**). Further deposition of an  $\text{HfO}_2$  protection layer outside of CdS/ $\text{HfO}_2$ /CZTS photocathode significantly increased its PEC stability (**Fig. S4**) while not decrease its PEC performances (**Fig. S3d**), the photocurrent density of the Pt- $\text{HfO}_2$ /CdS/ $\text{HfO}_2$ /CZTS photocathode was observed to be stable at about  $18 \text{ mA/cm}^2$  during 3 hours under AM 1.5G solar light irradiation (**Fig. S4**).

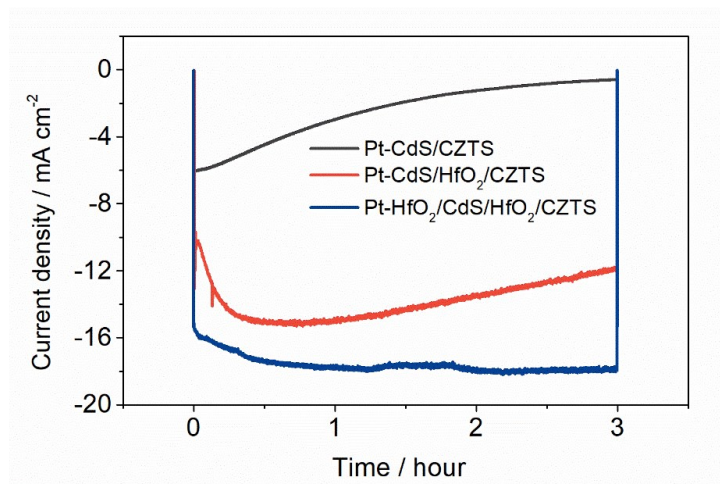


**Fig. S4:** Photocurrent density-time curves of Pt-CdS/CZTS, Pt-CdS/HfO<sub>2</sub>/CZTS and Pt-HfO<sub>2</sub>/CdS/HfO<sub>2</sub>/CZTS photocathodes.

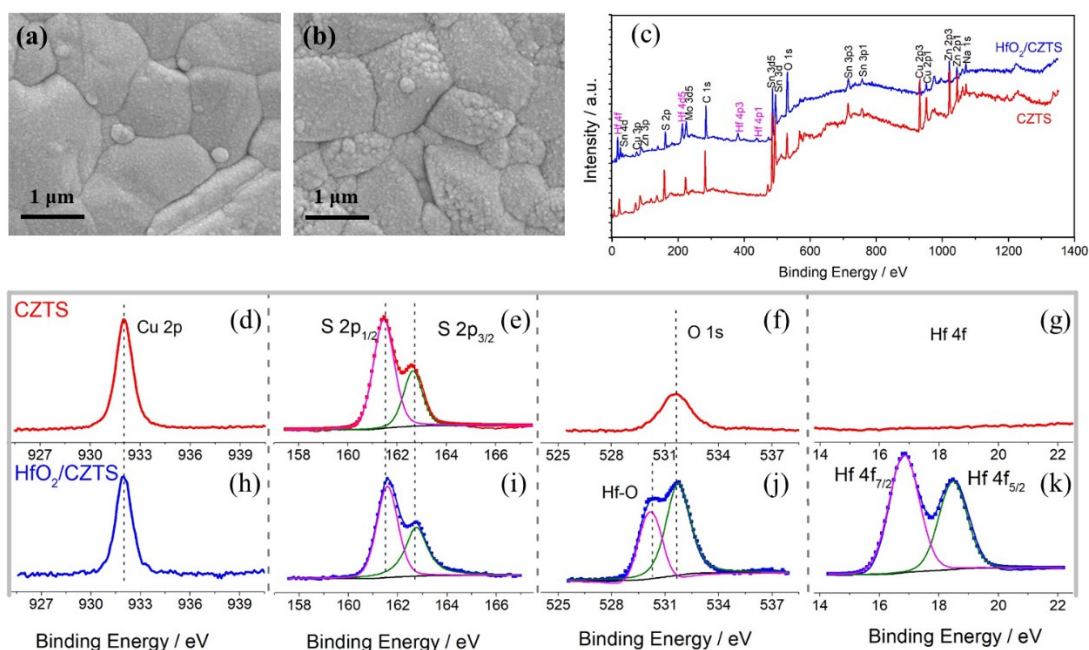


**Fig. S5:** SEM surface images of CdS/CZTS (a) and CdS/HfO<sub>2</sub>/CZTS (b) electrodes; full scan XPS spectra of CZTS and HfO<sub>2</sub>/CZTS films (c); normalized XPS spectra of Cu 2p (d), (h), S 2p (e), (i), O 1s (f), (j) and Hf 4f (g), (k) of CZTS and HfO<sub>2</sub>/CZTS films respectively.

Micro structure morphology of the CdS film deposited under bare CZTS and HfO<sub>2</sub>/CZTS film were shown in **Fig. S5a, b**. In generally, we did not observe any obvious difference in the morphology of them, numerous small CdS grains with a dense and continuous film structure fully passivated the surface of the CZTS large grains without any exposure. There is no difference in size/dispersion and density of the CdS

over layer deposited under CZTS film with and without HfO<sub>2</sub> modification. However, in order to confirm the modification of HfO<sub>2</sub> at the surface of CZTS, we used XPS for the identification by consideration its highly surface sensitive feature. Results shown in **Fig. S5c** confirmed the deposition of HfO<sub>2</sub> under CZTS film as we observed clear Hf 4f<sub>7/2</sub>, Hf 4f<sub>5/2</sub> and O 1s -Hf peaks from the CZTS sample with ALD HfO<sub>2</sub> modification (**Fig. S5j, k**). The position and intensity of the Cu 2p and S 2p peaks of the HfO<sub>2</sub>/CZTS sample are almost the same with that were detected from bare CZTS film (**Fig. S5d, e** and **h, i**), indicating the load intensity of HfO<sub>2</sub> is very low (most likely as several very small nanoparticles were loaded to CZTS) while CZTS was almost fully exposure without any obvious passivation. As likely to the previous discussion on the ALD Al<sub>2</sub>O<sub>3</sub> modified the CZTS grain boundaries,<sup>12,13</sup> we supposed that the HfO<sub>2</sub> may deposited at the grain boundary of CZTS, as shown in the diagram **Fig. S5b**, therefore we did not observe any obvious HfO<sub>2</sub> traces at the surface of CZTS. No Hf peak but a small O 1s peaks were observed from the bare CZTS sample, as shown in **Fig. S5f** and **g**, means several amounts of O<sub>2</sub> were easily to be absorbed at the surface of bare CZTS.

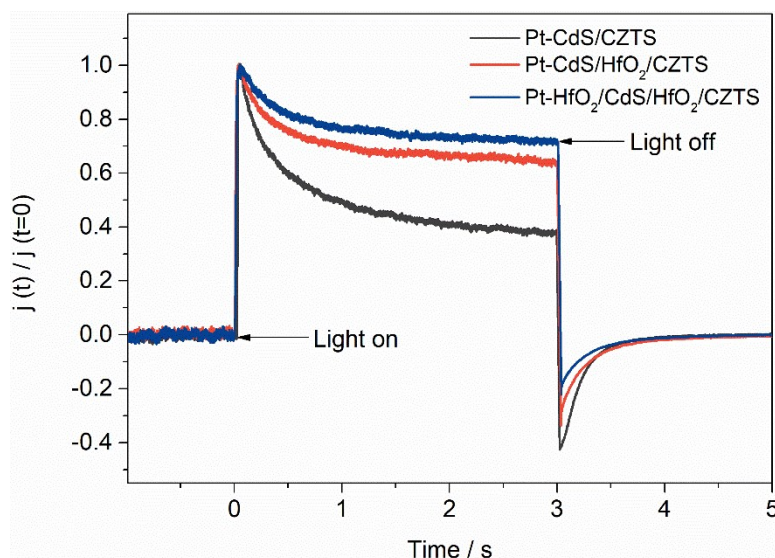


**Fig. S6:** Transit photocurrent spectrums of Pt-CdS/CZTS, Pt-CdS/HfO<sub>2</sub>/CZTS and Pt-HfO<sub>2</sub>/CdS/HfO<sub>2</sub>/CZTS photocathodes.

The transit photocurrent spectrums were carried out biased at 0.5 V<sub>RHE</sub> in 0.2 mol/dm<sup>3</sup> Na<sub>2</sub>HPO<sub>4</sub>/NaH<sub>2</sub>PO<sub>4</sub> buffer solution under AM 1.5G simulated sunlight

irradiation. As shown in **Fig. S6**, the Pt-HfO<sub>2</sub>/CdS/HfO<sub>2</sub>/CZTS photocathode possessed the smallest photocurrent spike and the slowest photocurrent decay, indicating that the CZTS-based photocathode buffered with the HfO<sub>2</sub>/CdS/HfO<sub>2</sub> sandwich structure layer presented a more effective charge transfer and a longer carrier lifetime than that of the Pt-CdS/CZTS and Pt-CdS/HfO<sub>2</sub>/CZTS photocathodes.

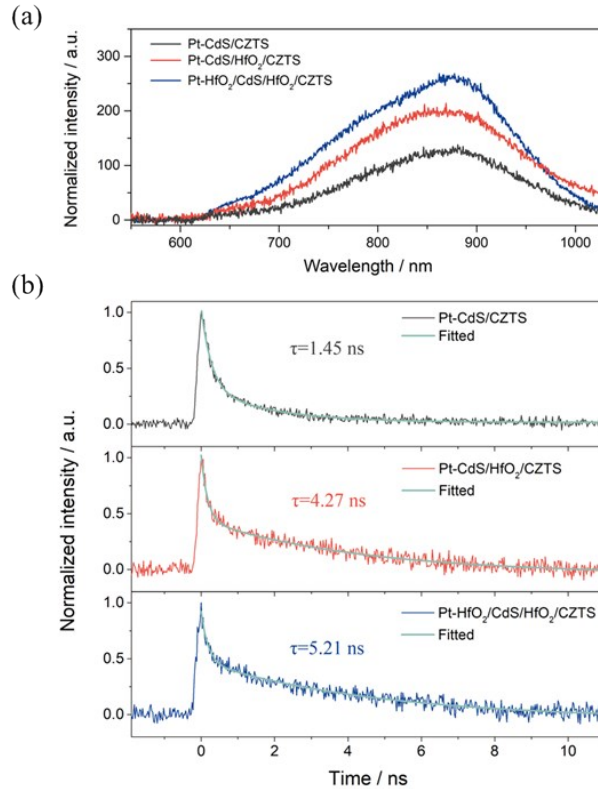


**Fig. S7:** Photoluminescence (PL) spectra (a) and corresponding time-resolved PL (TRPL) decay curves (b) for Pt-CdS/CZTS, Pt-CdS/HfO<sub>2</sub>/CZTS and Pt-HfO<sub>2</sub>/CdS/HfO<sub>2</sub>/CZTS photocathodes.

**Fig. S7a** shows the Steady-state photoluminescence (PL) spectra of Pt-CdS/CZTS, Pt-CdS/HfO<sub>2</sub>/CZTS and Pt-HfO<sub>2</sub>/CdS/HfO<sub>2</sub>/CZTS. The results indicate that the Pt-HfO<sub>2</sub>/CdS/HfO<sub>2</sub>/CZTS photocathode exhibited the highest overall PL intensity, which confirms that the HfO<sub>2</sub> overlayer under CdS buffer and HfO<sub>2</sub> insertion layer between CZTS and CdS buffer effectively passivate with respect to nonradiative recombination at the interfaces of Pt or electrolyte/CdS and CdS/CZTS, respectively.<sup>14</sup> Furthermore, time-resolved PL (TRPL) spectroscopy measurements were carried out to understand the underlying mechanism of the modified HfO<sub>2</sub>/CdS/HfO<sub>2</sub> sandwich buffer layer in

depth, results were shown in **Fig. S7b**. By fitting the TRPL spectra with a bi-exponential function model, we found that the average carrier lifetime increased from 1.45 ns to 4.27 ns and then to 5.21 ns with the introduction of the passivated HfO<sub>2</sub> insertion layer and outside overlayer, indicating that the carrier recombination at the two interfaces (Pt or electrolyte/CdS and CdS/CZTS) were well inhibited by such optimized passivation effect.<sup>15</sup>

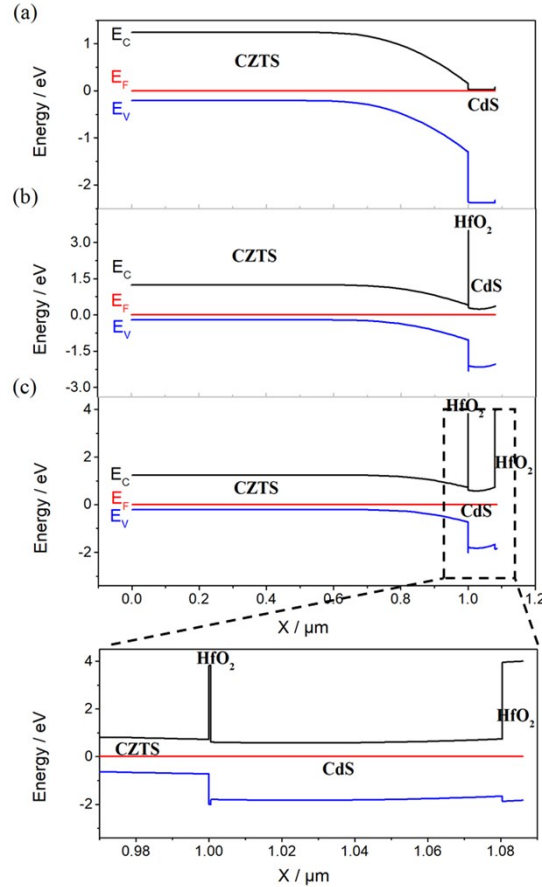


**Fig. S8:** Band schemas of CdS/CZTS (a), CdS/HfO<sub>2</sub>/CZTS (b) and HfO<sub>2</sub>/CdS/HfO<sub>2</sub>/CZTS (c) electrodes.

The band diagrams of CdS/CZTS, CdS/HfO<sub>2</sub>/CZTS and HfO<sub>2</sub>/CdS/HfO<sub>2</sub>/CZTS electrodes were simulated by SCAPS software, referring to the parameters of Wanda and Erkan et al.<sup>16-18</sup> As shown in **Fig. S8a**, there is a cliff-like conduction band offset (CBO, -0.12 eV) at the interface of CdS/CZTS, which is main cause of interface recombination, and further leads to the Voc limitation for photovoltaic device.<sup>16</sup> When we inserted an ultrathin HfO<sub>2</sub> layer, a large spike-like CBO (3.10 eV) and a large cliff-like CBO (-3.22 eV) was formed at the interface of CZTS/HfO<sub>2</sub> and HfO<sub>2</sub>/CdS,

respectively (**Fig. S8b**). Although the CBO values are extremely large, considering that the thickness of HfO<sub>2</sub> passivation layer is only 0.5 nm, which is not enough to affect the structure of space charge region. Photogenerated electrons can easily pass through this barrier and difficultly compound with holes.

On the other hand, a large valence band offset (VBO, -1.28 eV) at the interface of CZTS/HfO<sub>2</sub> may contribute to have a better selectivity for electrons in the heterojunction.<sup>13</sup> In addition, **Fig. S8c** shows another large CBO (3.22 eV) at the interface of outside HfO<sub>2</sub> layer and CdS. Similarly, photoelectrons can easily pass through this barrier to electrolyte and participate in HER reaction. Meanwhile, the HfO<sub>2</sub> passivation layer can absolutely insulate the CdS from the electrolyte and prevent the photocorrosion of CdS layer.<sup>19</sup>

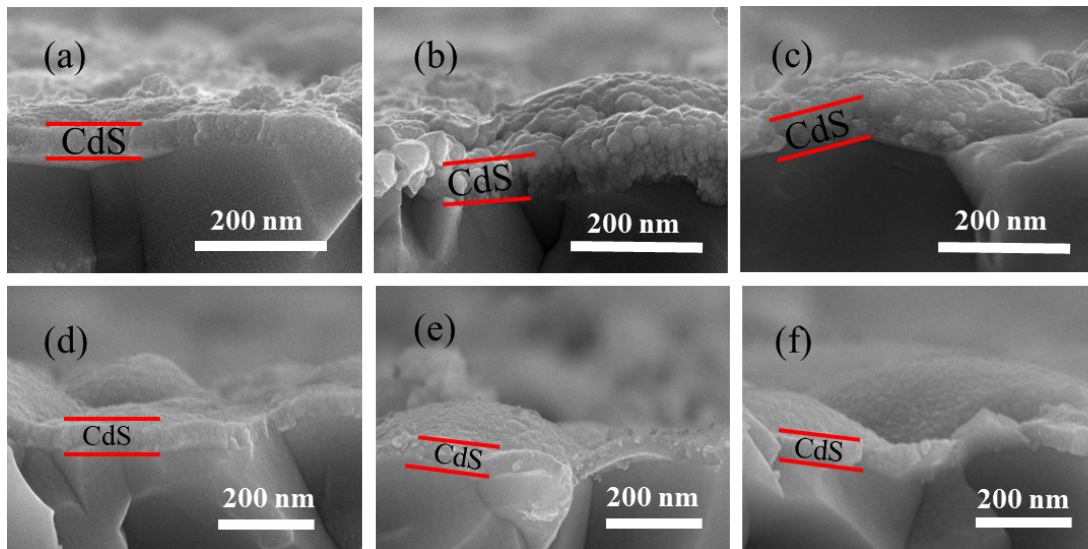


**Fig. S9:** Cross-sectional SEM images of Pt-CdS/CZTS and Pt-HfO<sub>2</sub>/CdS/HfO<sub>2</sub>/CZTS photocathodes undertaken before stability test (a), (d), after 6 hours stability test (b), (e) and after 12 hours stability test (c), (f), respectively.

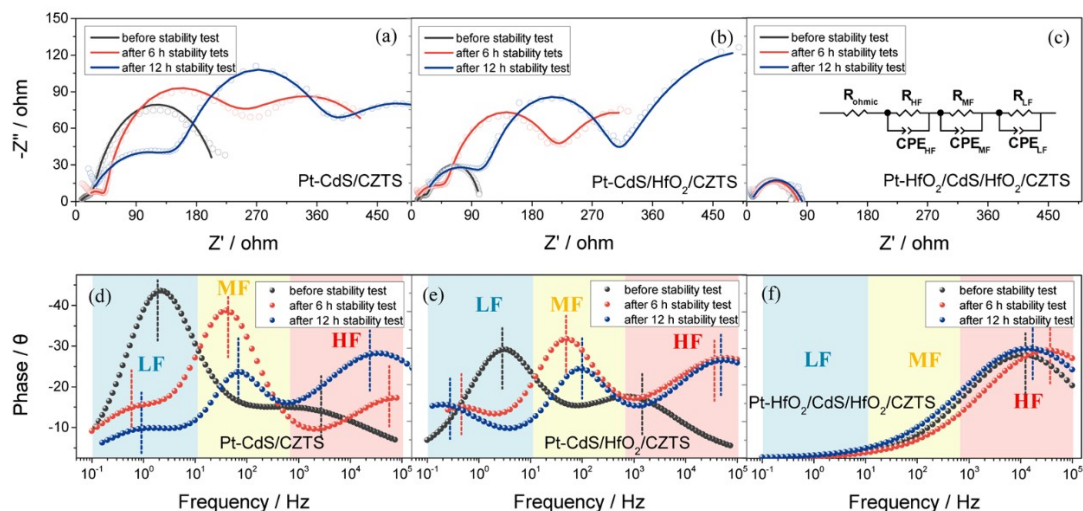


**Fig. S10:** Nyquist plots and corresponding Bode plots (biased at  $0.4 V_{\text{RHE}}$  under AM 1.5G light irradiation with the frequency range of 100 kHz to 0.1 Hz) measured at various stability test times (before stability test, after 6 hours stability test and after 12 hours stability test) of both Pt-CdS/CZTS (a) (d), Pt-CdS/HfO<sub>2</sub>/CZTS (b) (e) and Pt-HfO<sub>2</sub>/CdS/HfO<sub>2</sub>/CZTS (c) (f) photocathodes, respectively. In the Nyquist plots, scatter points represent the original experimental data, whereas solid lines represent fitted curves based on the equivalent circuit shown in the inset of (c).

An equivalent circuit model including three serially connected resistor–capacitor blocks with a resistance (R) and a constant phase element (CPE) at three different frequency ranges (inset of **Fig. S10c**) was used to analyze the EIS results. The physical meaning that the  $R_{\text{HF}}$ ,  $R_{\text{MF}}$  and  $R_{\text{LF}}$  presented or the relationship between these values and performances are already discussed previously.<sup>20</sup> It has been suggested that the high-frequency arc is influenced by the charge transport resistance within the electrode ( $R_{\text{HF}}$ ) with the capacitance of the bulk semiconductor ( $\text{CPE}_{\text{HF}}$ ) and the low-frequency arc represents the resistance of electrochemical charge-transfer reactions ( $R_{\text{LF}}$ , e.g., HER) with the capacitance of the electrode/electrolyte interface ( $\text{CPE}_{\text{LF}}$ ). An additional middle-frequency arc reflects the resistance ( $R_{\text{MF}}$ ) with the capacitance ( $\text{CPE}_{\text{MF}}$ ) of charge trapping at the surface trap states within the bandgap rather than charge-transfer reaction.<sup>20</sup>

**Table S1:** Fitted EIS resistance parameters of the Pt-CdS/CZTS, Pt-CdS/HfO<sub>2</sub>/CZTS and Pt-HfO<sub>2</sub>/CdS/HfO<sub>2</sub>/CZTS photocathodes.

Sample	$R_{\text{ohmic}} / \Omega \text{ cm}^2$	$R_{\text{HF}} / \Omega \text{ cm}^2$	$R_{\text{MF}} / \Omega \text{ cm}^2$	$R_{\text{LF}} / \Omega \text{ cm}^2$
Pt-CdS/CZTS before stability test	7.31	23.45	—	186.80
Pt-CdS/CZTS after 6 h stability test	12.87	31.84	172.44	281.52
Pt-CdS/CZTS after 12 h stability test	16.76	157.50	192.10	303.38
Pt-CdS/HfO <sub>2</sub> /CZTS before stability test	7.68	17.09	—	76.72
Pt-CdS/HfO <sub>2</sub> /CZTS after 6 h stability test	8.56	52.08	157.32	189.88
Pt-CdS/HfO <sub>2</sub> /CZTS after 12 h stability test	16.23	102.08	181.61	358.16
Pt-HfO <sub>2</sub> /CdS/HfO <sub>2</sub> /CZTS before stability test	6.31	64.89	—	—
Pt-HfO <sub>2</sub> /CdS/HfO <sub>2</sub> /CZTS after 6 h stability test	7.09	70.53	—	—
Pt-HfO <sub>2</sub> /CdS/HfO <sub>2</sub> /CZTS after 12 h stability test	6.53	76.38	—	—

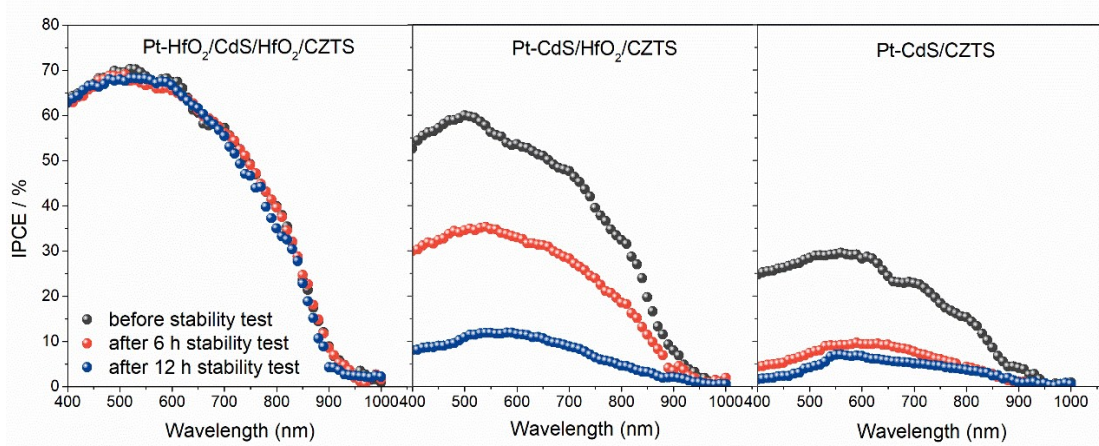


**Fig. S11:** IPCE spectrums of Pt-HfO<sub>2</sub>/CdS/HfO<sub>2</sub>/CZTS, Pt-CdS/HfO<sub>2</sub>/CZTS and Pt-CdS/CZTS photocathodes under 0 V<sub>RHE</sub> with different stability test times (before stability test, after 6 hours stability test and after 12 hours stability test).

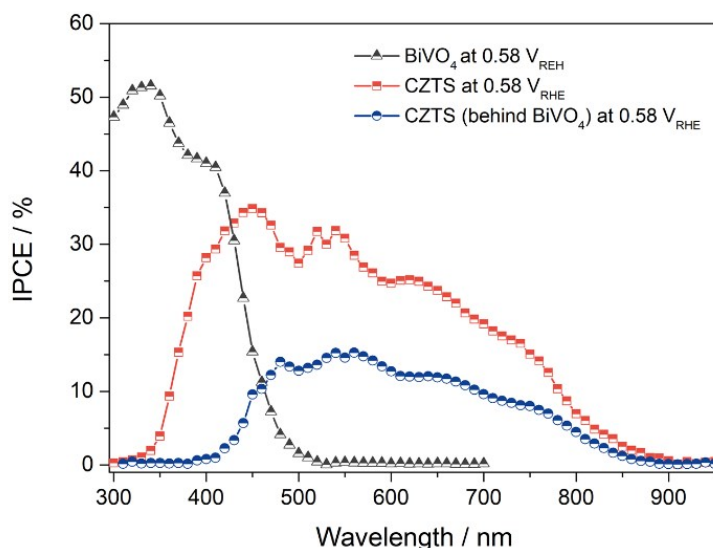


**Fig. S12:** IPCE spectra of the CZTS photocathode, BiVO<sub>4</sub> photoanode and CZTS photocathode behind the BiVO<sub>4</sub> photoanode.

The IPCE spectrums (shown in **Fig. S12**) were measured under 0.58 V<sub>RHE</sub>: the BiVO<sub>4</sub> photoanode presented an obvious sharp decrease in IPCE spectrum around at 400-500 nm due to its bandgap limitation. While the CZTS-based photocathode exhibited a step increment in IPCE response after about 400 nm. This result indicates that the two electrodes show complimentary spectral responses.

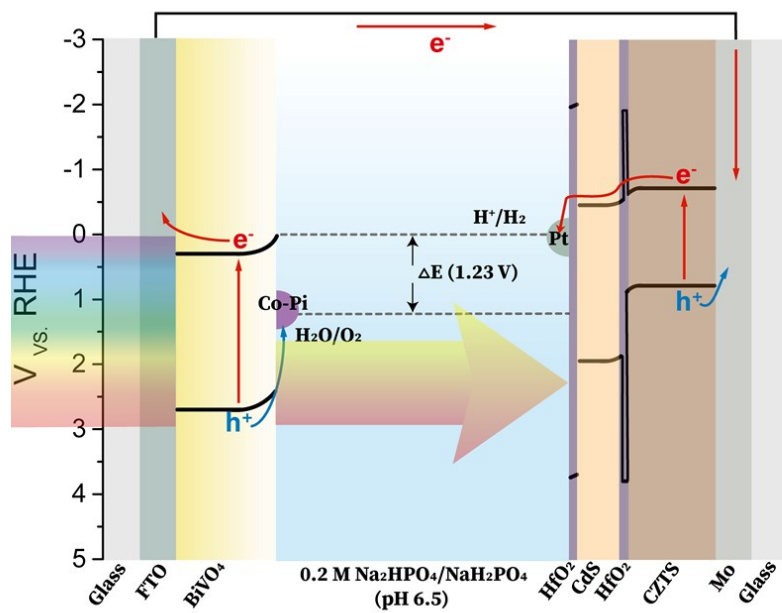


**Fig. S13:** Energy diagram of CZTS-BiVO<sub>4</sub> tandem device for unbiased water splitting in pH 6.5 buffer solution.



**Fig. S14:** Outdoor working surroundings for large area (5×5cm) integrated CZTS-BiVO<sub>4</sub> tandem device.

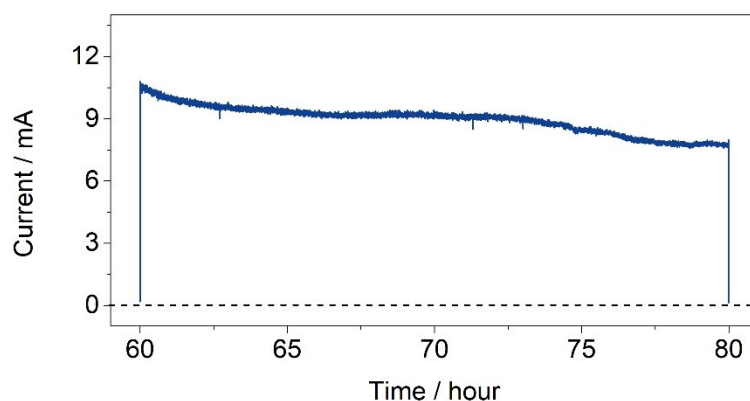


**Fig. S15:** Later 20-hour current-time curves of the 5×5cm size integrated CZTS-BiVO<sub>4</sub> tandem device after the 60-hour stability test shown in **Fig. 5g**.

As shown in **Fig. S15**, the photocurrent of the 5×5cm size integrated CZTS-BiVO<sub>4</sub> tandem device further gradually decreased. According to our experimental experience, we found that the decreased photocurrent of the CZTS would be significantly recovered after we again photoelectrochemical deposited fresh Pt catalysts under the CZTS photoelectrode. The gradual detachment of Pt catalyst during the working stage is one of the reasons why the photocurrent decreased gradually. This phenomenon also be found by Jooho Moon et al.,<sup>21</sup> they thought that the detachment of Pt particles due to the releasing of large bubbles is one of the well-known degradation mechanisms in the Pt-decorated photocathodes for solar water splitting. Meanwhile, the electrolyte that continuously heated up by the simulated sunlight irradiation may further accelerate the CdS photocorrosion process. Notably, the moderate pH environments (pH=6.5) in this stability test may be not very appropriate for the BiVO<sub>4</sub> photoanode,<sup>22</sup> which may result in the instability of this large size tandem device.

Based on these speculations and discussions, many strategies can be carried out to improve the PEC stability for future development of this large size tandem cell. First, enhancing adhesion between the catalyst and protective layers could improve the stability of photocathodes.<sup>22</sup> For instance, Rojas et al. coated a solution processed polyethyleneimine (PEI) on top of Pt catalysts to prevent the delamination, as a result, the stability of the photocathodes was much improved.<sup>22</sup> Furthermore, a constant relatively low temperature reaction condition is necessary to delay the photocorrosion, when the stability of the tandem device is evaluated. Moreover, regulating the

electrolyte composition and controlling the dissolution during the PEC reaction has become an increasingly attractive strategy to improve the stability of PEC system.<sup>22</sup> For example, Moon et al. added some amount of  $V^{5+}$  of the form  $V_2O_5$  into the moderate pH electrolyte (pH=7) to improve the stability of the  $BiVO_4$  photoanode and further improve the PEC stability of their photocathode-photoanode tandem cell.<sup>21</sup> Consequently, further significant enhancement in the durability of this large size CZTS- $BiVO_4$  tandem cell is very promising.

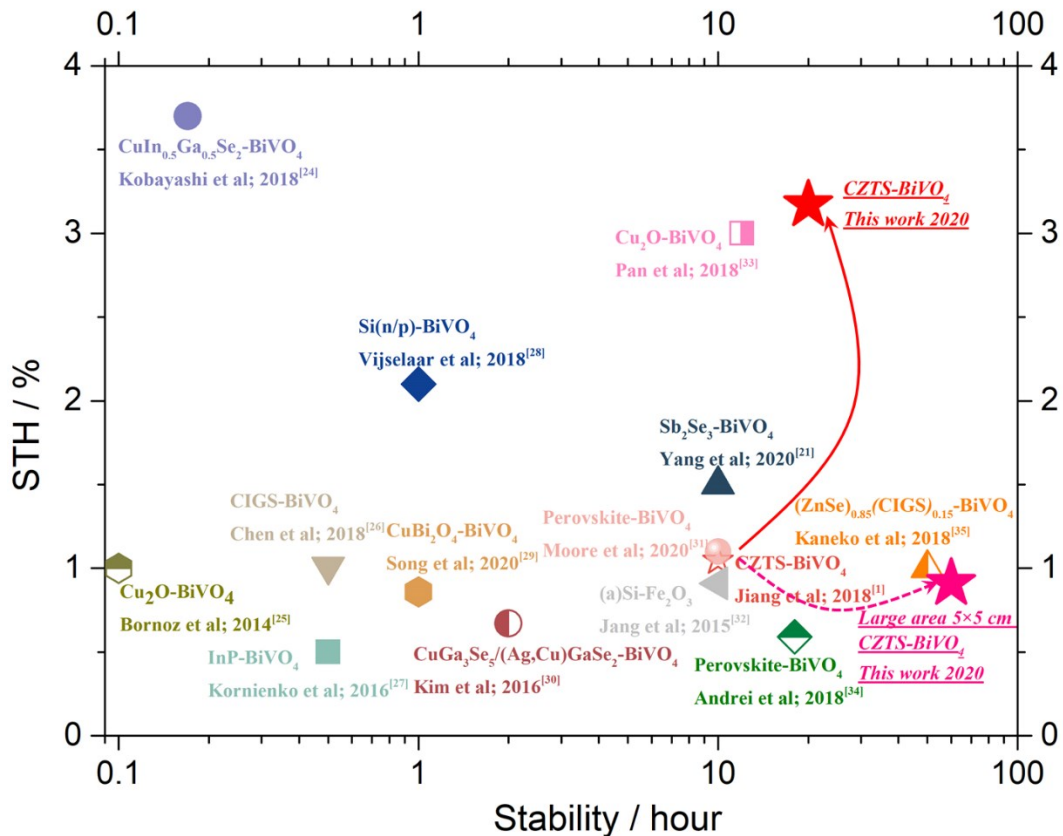


**Fig. S16:** Efficiency and stability benchmarks for previously reported typical photoanode–photocathode tandem device.

As compare with previously reported typical photoanode-photocathode tandem cells, it was found that the  $CZTS-BiVO_4$  tandem cell in this work showed a very high efficiency that was close to the world record value from  $CuIn_{0.5}Ga_{0.5}Se_2-BiVO_4$  tandem cell (Kobayashi et al. 2018)<sup>24</sup>. Meanwhile, the  $CZTS-BiVO_4$  tandem cell exhibited a longest stability over 60hours that was even longer than  $(ZnSe)_{0.85}(CIGS)_{0.15}-BiVO_4$  tandem cell (Kaneko et al. 2018)<sup>35</sup>. Notably, the use of toxic elements In and Se and

the expensive component Ga are significant drawbacks for CIGS-based tandem devices. But CZTS-based tandem devices exhibit lower cost and environmentally friendly characteristics, are more suitable for practical applications. Furthermore, the large scale CZTS-BiVO<sub>4</sub> tandem cell (5×5 cm) showed a longest stability of 60 hours. This is a significant progress of photoanode-photocathode tandem device for overall water splitting.

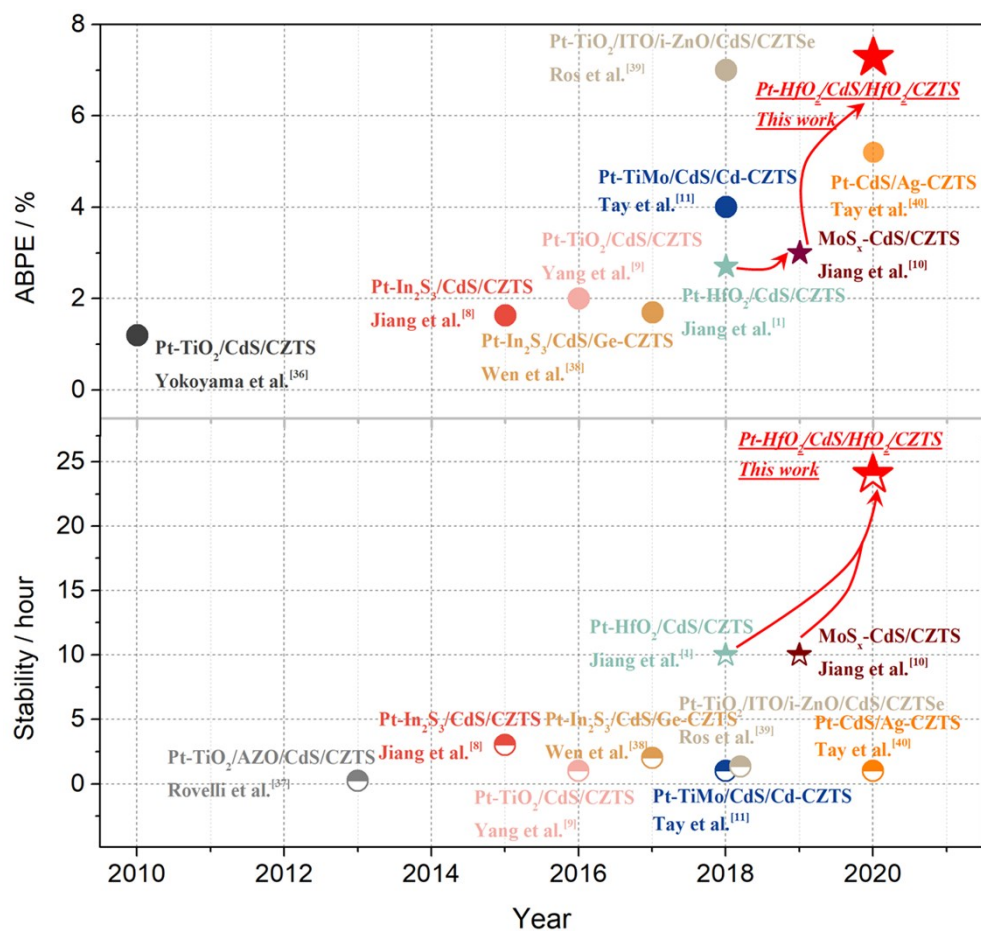


**Fig. S17:** Efficiency and stability benchmarks for previously reported CZTS-based photocathode.

As compare with previously reported CZTS-based photocathode, it was found that the CZTS-based photocathode modified by HfO<sub>2</sub>/CdS/HfO<sub>2</sub> sandwich buffer layers in this work showed a record ABPE of 7.27% and a longest stability of 24 hours up to now.

Although the 24 hours longest stability of our revised CZTS-based photocathode

still has distance from the truly stable system, 24 hours stability is a great progress for CZTS-based photocathode up to now. Meanwhile, the application of HfO<sub>2</sub>/CdS/HfO<sub>2</sub> sandwich buffer layer could open a new avenue to improve the stability of other kinds of photocathodes. As a result, we believe that our new strategy will significantly contribute to the PEC water splitting field.

Severe photocorrosion in the CdS buffer layer is the main reason of the instability of CZTS based PEC water splitting device, adding a surface protection layer under CdS buffer to inhibit the photocorrosion is an efficient way to make the photoelectrode stable.<sup>1,8</sup> Further investigate suitable protection layer under CdS buffer or search stable but efficient buffer to replace CdS buffer to fabricate CdS free CZTS photoelectrode should be promising to largely enhance the stability. Recently Moon et al. found that the detachment of surface catalysts or the catalyst poisoning is also the important reason for the low PEC stability for various photocathodes.<sup>21</sup> The catalysts (Pt nano particles) was photodeposited under the surface of CZTS based photocathode, we believe that the Pt catalysts should be inhomogeneous dispersed at the surface of photoelectrode. Some Pt big cluster catalysts may easy to be detached from the electrode surface, and the combination between Pt nanoparticle catalysts to the electrode surface i.e. CdS buffer or HfO<sub>2</sub>/CdS/HfO<sub>2</sub> buffer is not strong, the structure of thus surface nanoparticle catalysts/multilayer film may not the best architecture for the long time PEC stability of CZTS photoelectrode. Reconstruct stable catalyst/photoelectrode interfacial structure should be the key point to efficiently improve the CZTS based photoelectrode. Further investigations on the way.

**Table S2.** Statistics data of photoelectrochemical performances of typical CZTS-based photocathode up to now.

CZTS-based Photocathode	pH of electrolyte	Photocurrent density/mA cm <sup>-2</sup>	Onset potential/ V <sub>RHE</sub>	ABPE	Stability (retention)	Reference; year
<b>Pt-HfO<sub>2</sub>/CdS/HfO<sub>2</sub>/CZTS</b>	<b>6.5</b>	<b>-18 (0 V<sub>RHE</sub>)</b>	<b>0.71</b>	<b>5.57%</b>	<b>24 hours (97%)</b>	<b>this work; 2020</b>
<b>Pt-HfO<sub>2</sub>/CdS/HfO<sub>2</sub>/CZTS</b>	<b>3.0</b>	<b>-28 (0 V<sub>RHE</sub>)</b>	<b>0.72</b>	<b>7.27%</b>	<b>3 hours (86%)</b>	<b>this work; 2020</b>
Pt-TiO <sub>2</sub> /CdS/CZTS	9.5	-9 (0 V <sub>RHE</sub> )	0.6	1.2%	N/A	Yokoyama et al; 2010 <sup>[36]</sup>
Pt-CdS/CZTS	9.0	-2.5 (0 V <sub>RHE</sub> )	0.45	N/A	N/A	Ma et al; 2011 <sup>[41]</sup>
Pt-TiO <sub>2</sub> /AZO/CdS/CZTS	7.0	-1 (0 V <sub>RHE</sub> )	0.2	N/A	0.25 hour (55%)	Rovelli et al; 2013 <sup>[37]</sup>
Pt-In <sub>2</sub> S <sub>3</sub> /CdS/CZTS	6.5	-9.3 (0 V <sub>RHE</sub> )	0.6	1.63%	3 hours (100%)	Jiang et al; 2015 <sup>[8]</sup>
Pt-TiO <sub>2</sub> /CdS/CZTS	6.85	-11 (0 V <sub>RHE</sub> )	0.6	2%	1 hour (60%)	Yang et al; 2016 <sup>[9]</sup>
Pt-In <sub>2</sub> S <sub>3</sub> /CdS/Ge-CZTS	6.5	-11.1 (0 V <sub>RHE</sub> )	0.61	1.7%	2 hours (90%)	Wen et al; 2017 <sup>[38]</sup>
Pt-TiMo/CdS/Cd-CZTS	6.5	-17 (0 V <sub>RHE</sub> )	0.6	4%	1 hour (90%)	Tay et al; 2018 <sup>[11]</sup>
Pt-HfO <sub>2</sub> /CdS/CZTS	6.5	-12 (0 V <sub>RHE</sub> )	0.65	2.7%	10 hours (90%)	Jiang et al; 2018 <sup>[1]</sup>
Pt-TiO <sub>2</sub> /ITO/i-ZnO/CdS/CZTSe	1.0	-37 (0 V <sub>RHE</sub> )	0.45	7%	1.3 hours (93%)	Ros et al; 2018 <sup>[39]</sup>
MoS <sub>x</sub> -CdS/CZTS	3.0	-18 (0 V <sub>RHE</sub> )	0.6	3%	10 hours (70%)	Jiang et al; 2019 <sup>[10]</sup>
Pt-CdS/Ag-CZTS	7.0	-17.7 (0 V <sub>RHE</sub> )	0.85	5.2%	1 hour (80%)	Tay et al; 2020 <sup>[40]</sup>

## References

1. Huang, D. et al. Over 1% efficient unbiased stable solar water splitting based on a sprayed  $\text{Cu}_2\text{ZnSnS}_4$  photocathode protected by a  $\text{HfO}_2$  photocorrosion-resistant film. *ACS Energy Lett.* **3**, 1875-1881 (2018).
2. Nguyen, T.H. et al. Structural and solar cell properties of a Ag-containing  $\text{Cu}_2\text{ZnSnS}_4$  thin film derived from spray pyrolysis. *ACS Appl. Mater. Interfaces* **10**, 5455-5463 (2018).
3. Kuang, Y.B. et al. A front-illuminated nanostructured transparent  $\text{BiVO}_4$  photoanode for > 2% efficient water splitting. *Adv. Energy Mater.* **6**, 1501645 (2016).
4. Abdi, F.F. et al. Efficient solar water splitting by enhanced charge separation in a bismuth vanadate-silicon tandem photoelectrode. *Nat. Commun.* **4**, 2195 (2013).
5. Abdi, F.F. & van de Krol, R. Nature and light dependence of bulk recombination in Co-Pi-catalyzed  $\text{BiVO}_4$  photoanodes. *J. Phys. Chem. C* **116**, 9398-9404 (2012).
6. Wang, D., He, G., Hao, L., Gao, J. & Zhang, M. Comparative passivation effect of ALD-driven  $\text{HfO}_2$  and  $\text{Al}_2\text{O}_3$  buffer layers on the interface chemistry and electrical characteristics of Dy-based gate dielectrics. *J. Mater. Chem. C* **7**, 1955-1965 (2019).
7. Xing, Z. et al. Enhanced PEC performance of nanoporous Si photoelectrodes by covering  $\text{HfO}_2$  and  $\text{TiO}_2$  passivation layers. *Sci. Rep.* **7**, 43901 (2017).
8. Jiang, F. et al. Pt/ $\text{In}_2\text{S}_3$ / $\text{CdS}/\text{Cu}_2\text{ZnSnS}_4$  thin film as an efficient and stable photocathode for water reduction under sunlight radiation. *J. Am. Chem. Soc.* **137**, 13691-13697 (2015).
9. Yang, W. et al. Molecular chemistry-controlled hybrid ink derived efficient  $\text{Cu}_2\text{ZnSnS}_4$  photocathodes for photoelectrochemical water splitting. *ACS Energy Lett.* **1**, 1127-1136 (2016).
10. Feng, K. et al.  $\text{MoS}_x$ - $\text{CdS}/\text{Cu}_2\text{ZnSnS}_4$ -based thin film photocathode for solar hydrogen evolution from water. *Appl. Catal. B: Environ.* **268**, 118438 (2020).
11. Tay, Y.F. et al. Solution-processed Cd-substituted CZTS photocathode for efficient solar hydrogen evolution from neutral water. *Joule* **2**, 537-548 (2018).
12. Park, J. et al. The role of hydrogen from ALD- $\text{Al}_2\text{O}_3$  in kesterite  $\text{Cu}_2\text{ZnSnS}_4$  solar cells: grain surface passivation. *Adv. Energy Mater.* **8**, 1701940 (2018).
13. Ojeda-Duran, E. et al. CZTS solar cells and the possibility of increasing  $V_{OC}$  using evaporated  $\text{Al}_2\text{O}_3$  at the CZTS/ $\text{CdS}$  interface. *Sol. Energy* **198**, 696-703 (2020).
14. Sun, K.W. et al. Self-assembled nanometer-scale ZnS structure at the CZTS/ $\text{ZnCdS}$  heterointerface for high-efficiency wide band gap  $\text{Cu}_2\text{ZnSnS}_4$  solar cells. *Chem. Mater.* **30**, 4008-4016 (2018).
15. Chen, M.X. et al. Spatial control of cocatalysts and elimination of interfacial defects towards efficient and robust CIGS photocathodes for solar water splitting. *Energy Environ. Sci.* **11**, 2025-2034 (2018).
16. Wanda, M.D., Ouedraogo, S., Tchoffo, F., Zougmore, F. & Ndjaka, J.M.B. Numerical investigations and analysis of  $\text{Cu}_2\text{ZnSnS}_4$  based solar cells by SCAPS-1D. *Int. J. Photoenergy* **2016**, 2152018 (2016).
17. Erkan, M.E., Chawla, V. & Scarpulla, M.A.. Reduced defect density at the CZTSSe/ $\text{CdS}$  interface by atomic layer deposition of  $\text{Al}_2\text{O}_3$ . *J. Appl. Phys.* **119**, 194504 (2016).
18. Marlein, J., Decock, K. & Burgelman, M. Analysis of electrical properties of CIGSSe and Cd-free buffer CIGSSe solar cells. *Thin Solid Films* **517**, 2353-2356 (2009).
19. Liu, R., Zheng, Z., Spurgeon, J. & Yang, X. Enhanced photoelectrochemical water-splitting performance of semiconductors by surface passivation layers. *Energy Environ. Sci.* **7**, 2504-2517 (2014).
20. Tan, J. et al. Fullerene as a photoelectron transfer promoter enabling stable  $\text{TiO}_2$ -protected  $\text{Sb}_2\text{Se}_3$

- photocathodes for photo-electrochemical water splitting. *Adv. Energy Mater.* **9**, 1900179 (2019).
21. Yang, W. et al. Benchmark performance of low-cost  $\text{Sb}_2\text{Se}_3$  photocathodes for unassisted solar overall water splitting. *Nat. Commun.* **11**, 861 (2020).
  22. Yang, W., Prabhakar, R.R., Tan, J., Tilley, S.D. & Moon, J. Strategies for enhancing the photocurrent, photovoltage, and stability of photoelectrodes for photoelectrochemical water splitting. *Chem. Soc. Rev.* **48**, 4979-5015 (2019).
  23. Rojas, H.C. et al. Polymer-based photocathodes with a solution-processable cuprous iodide anode layer and a polyethyleneimine protective coating. *Energy Environ. Sci.* **9**, 3710-3723 (2016).
  24. Kobayashi, H. et al. Development of highly efficient  $\text{CuIn}_{0.5}\text{Ga}_{0.5}\text{Se}_2$ -based photocathode and application to overall solar driven water splitting. *Energy Environ. Sci.* **11**, 3003-3009 (2018).
  25. Borno, P. et al. A bismuth vanadate-cuprous oxide Tandem cell for overall solar water splitting. *J. Phys. Chem. C* **118**, 16959-16966 (2014).
  26. Chen, M.X. et al. Spatial control of cocatalysts and elimination of interfacial defects towards efficient and robust CIGS photocathodes for solar water splitting. *Energy Environ. Sci.* **11**, 2025-2034 (2018).
  27. Kornienko, N. et al. Growth and photoelectrochemical energy conversion of wurtzite indium phosphide nanowire arrays. *ACS Nano* **10**, 5525-5535 (2016).
  28. Vijselaar, W. et al. Spatial decoupling of light absorption and catalytic activity of Ni-Mo-loaded high-aspect-ratio silicon microwire photocathodes. *Nat. Energy* **3**, 185-192 (2018).
  29. Song, A.G. et al. Assessment of a  $\text{W}:\text{BiVO}_4\text{-CuBi}_2\text{O}_4$  tandem photoelectrochemical cell for overall solar water splitting. *ACS Appl. Mater. Interfaces* **12**, 13959-13970 (2020).
  30. Kim, J.H. et al. Overall photoelectrochemical water splitting using tandem cell under simulated sunlight. *ChemSusChem* **9**, 61-66 (2016).
  31. Moore, E.E., Andrei, V., Zacarias, S., Pereira, I.A.C. & Reisner, E. Integration of a hydrogenase in a lead halide perovskite photoelectrode for tandem solar water splitting. *ACS Energy Lett.* **5**, 232-237 (2020).
  32. Jang, J.W. et al. Enabling unassisted solar water splitting by iron oxide and silicon. *Nat. Commun.* **6**, 7447 (2015).
  33. Pan, L. et al. Boosting the performance of  $\text{Cu}_2\text{O}$  photocathodes for unassisted solar water splitting devices. *Nat. Catal.* **1**, 412-420 (2018).
  34. Andrei, V. et al. Scalable triple cation mixed halide perovskite- $\text{BiVO}_4$  tandems for bias-free water splitting. *Adv. Energy Mater.* **8**, 1801403 (2018).
  35. Kaneko, H., Minegishi, T., Kobayashi, H., Kuang, Y. & Domen, K. Suppression of poisoning of photocathode catalysts in photoelectrochemical cells for highly stable sunlight-driven overall water splitting. *J. Chem. Phys.* **150**, 041713 (2019).
  36. Yokoyama, D. et al.  $\text{H}_2$  evolution from water on modified  $\text{Cu}_2\text{ZnSnS}_4$  photoelectrode under solar light. *Appl. Phys. Express* **3** 101202 (2010).
  37. Rovelli, L., Tilley, S.D. & Sivula, K. Optimization and stabilization of electrodeposited  $\text{Cu}_2\text{ZnSnS}_4$  photocathodes for solar water reduction. *ACS Appl. Mater. Interfaces* **5**, 8018-8024 (2013).
  38. Wen, X., Luo, W.J., Guan, Z.J., Huang, W., & Zou, Z.G. Boosting efficiency and stability of a  $\text{Cu}_2\text{ZnSnS}_4$  photocathode by alloying Ge and increasing sulfur pressure simultaneously. *Nano Energy* **41**, 18-26 (2017).
  39. Ros, C. et al. Turning earth abundant kesterite-based solar cells into efficient protected water-splitting photocathodes. *ACS Appl. Mater. Interfaces* **10**, 13425-13433 (2018).
  40. Tay, Y.F. et al. Improving the interfacial properties of CZTS photocathodes by Ag substitution. *J.*

*Mater. Chem. A* **8**, 8862-8867 (2020).

41. Ma, G., Minegishi, T., Yokoyama, D., Kubota, J. & Domen, K. Photoelectrochemical hydrogen production on  $\text{Cu}_2\text{ZnSnS}_4/\text{Mo}$ -mesh thin-film electrodes prepared by electroplating. *Chem. Phys. Lett.* **501**, 619-622 (2011).